Parameterization of Vertical Turbulent Transport in the Inner Core of Tropical Cyclones and Its Impact on Storm Intensification. Part II: Understanding TC Intensification in a Generalized Sawyer–Eliassen Diagnostic Framework

JEREMY KATZ[a] AND PING ZHU[a]

[a] *Department of Earth and Environment, Florida International University, Miami, Florida*

(Manuscript received 22 December 2023, in final form 23 August 2024, accepted 9 September 2024)

ABSTRACT: An analytical method for diagnosing the interaction between the primary and secondary circulations of a tropical cyclone (TC) and vortex intensification is developed. It includes a diagnostic equation describing the mean secondary circulation of a TC in an unbalanced framework by including the radial eddy forcing in the analytical system. It is an extension of the Sawyer–Eliassen equation (SEE) developed from the strict gradient-wind balance. This generalized SEE (GSEE) remediates some of the limitations of SEE and can be used to diagnose both balanced and unbalanced dynamical processes during the TC evolution. Using GSEE, this study investigates how the tangential and radial eddy forcing affects the TC intensification simulated by the Hurricane Weather Research and Forecasting Model (HWRF) with differently parameterized turbulent mixing. The diagnostic results show that the supergradient component of radial eddy forcing contributes positively to the acceleration of the peak tangential wind, whereas the subgradient component of the radial eddy forcing tends to lower the height of peak tangential wind. The relative importance of negative and positive effects of tangential eddy forcing on TC intensification varies depending on the details of turbulence parameterization. For a turbulent kinetic energy (TKE) scheme used in this study, a large sloping curvature of mixing length in the low troposphere causes the tangential eddy forcing to produce a net positive tangential wind tendency near the location of the peak tangential wind. In contrast, a small sloping curvature of mixing length generates a net negative tangential wind tendency at the peak tangential wind.

SIGNIFICANCE STATEMENT: The interaction between the primary and secondary circulations of a tropical cyclone (TC) plays a key role in TC evolution. Historically, the secondary circulation induced by turbulence and convection is often described by a so-called Sawyer–Eliassen equation (SEE). While SEE has provided much insight into the TC dynamics in the past, the assumption of gradient-wind balance used by SEE prevents it from understanding TC unbalanced dynamics. To remediate the limitation, we extended the analytical framework into the unbalanced regime by including radial eddy forcing in the analytical system and derived a generalized SEE (GSEE). Using GSEE, this study investigates how tangential and radial eddy forcing affects TC intensification. The result highlights the importance of multiple roles that turbulence plays in the intensification of TCs.

KEYWORDS: Turbulence; Tropical cyclones; Numerical analysis/modeling; Parameterization

1. Introduction

To the first-order approximation, a tropical cyclone (TC) vortex can be described by the gradient-wind balance. In the boundary layer (BL), the friction induced by the turbulence slows down the TC tangential wind, so that the outward Coriolis force and centrifugal force can no longer balance the inward pressure gradient force. This results in the radial inflow in the BL. As the air converges toward the storm center, it erupts out of the BL and diverges out along the eyewall known as the Ekman pumping as illustrated by Fig. 1. While most part of the BL in the TC inner core is subgradient due to the slowdown of tangential winds by turbulent friction, the air near the outflow region in the upper part of the BL (indicated by the gray cycles in Fig. 1) is actually supergradient. Based on this unique inflow and outflow structure, Smith et al. (2009) divided the TC inner core into two regions (regions A and B in Fig. 1) and argued that the interaction between the BL and the free vortex above mainly takes place in region B where the air in the BL is pumped into the free vortex, and thus, it exerts a profound impact on vortex structure and intensification. It is also important to point out that the BL becomes ill defined in this region as no physical interface exists to separate the turbulence generated by the BL processes and cloud processes aloft in the eyewall. Thus, the treatment of turbulent mixing must go beyond the conventional scope of the BL in the TC inner core (Zhu et al. 2019, 2021).

While the difference of the BL processes in different regions has been recognized, the details of how the unbalanced dynamics resulting from BL turbulence and convection affects TC intensification remain poorly understood as we lack an appropriate

Denotes content that is immediately available upon publication as open access.

Supplemental information related to this paper is available at the Journals Online website: https://doi.org/10.1175/JAS-D-23-0243.s1.

Corresponding author: Ping Zhu, zhup@fiu.com

DOI: 10.1175/JAS-D-23-0243.1

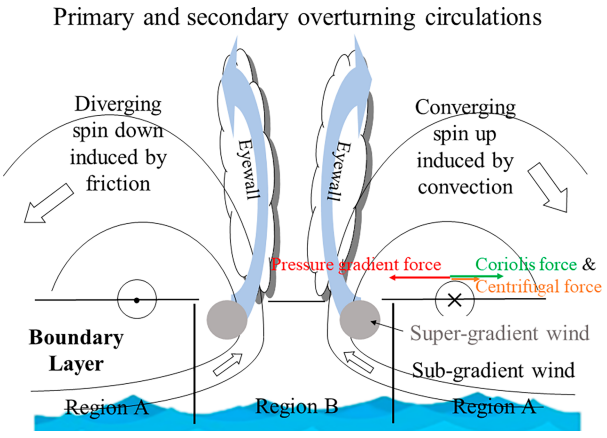

FIG. 1. A schematic illustration of the interaction among the primary TC vortex, secondary overturning circulation, surface friction, diabatic heating of convection, and turbulent transport in the eyewall during the evolution of a TC vortex.

diagnostic tool that can be used to analyze numerical simulation output and quantify the contribution of individual unbalanced processes to vortex intensification. A TC vortex is assumed to satisfy both gradient-wind balance and hydrostatic balance. Shapiro and Willoughby (1982) first showed that the secondary overturning circulation of a TC vortex can be analytically described by an elliptical partial differential equation known as Sawyer–Eliassen equation (SEE). SEE is a powerful mathematical tool for diagnosing a TC vortex as it provides a way to quantify contributions from individual processes of diabatic heating and tangential turbulent eddy forcing to the acceleration/deceleration of the primary circulation by combining it with the tangential wind budget equation. However, the assumption of strict gradient wind balance of SEE prevents it from diagnosing the contributions of unbalanced processes to the TC intensification. To date, no SEE-like diagnostic equation has been derived in an unbalanced TC framework, and this motivates us to develop a new diagnostic tool that can be used to quantify the contributions of individual unbalanced turbulent processes to TC intensification. Utilizing the developed diagnostic tool, we attempt to address some of the unanswered questions regarding the impact of parameterized turbulent eddy forcing on TC intensification in numerical simulations.

This paper is organized as follows. In section 2, a generalized SEE-like equation in an unbalanced framework is derived. This equation along with the tangential wind budget equation is, then, used to diagnose the vortex intensification in the idealized TC simulations by the Hurricane Weather Research and Forecasting Model (HWRF) described in section 3. The analysis results are presented in section 4 followed by a summary of this study in section 5.

2. A generalized Sawyer–Eliassen equation

The azimuth-mean tangential wind budget equation in a storm-centered cylindrical coordinate may be written as

$$\frac{\partial \overline{v_t}}{\partial t} = -\overline{u_r}\overline{\xi} - \overline{w}\frac{\partial \overline{v}_t}{\partial z} + F_\lambda + F_{\mathrm{sgs}_\lambda},$$

$$F_\lambda = -\overline{u_r'\zeta'} - \overline{v_t'\frac{\partial v_t'}{r\partial\lambda}} - \overline{w'\frac{\partial v_t'}{\partial z}}, \tag{1}$$

where r, λ, and z are the axes in the radial, azimuthal, and vertical direction, respectively; u_r, v_t, and w are the radial, tangential, and vertical wind components; overbar and prime indicate the azimuthal mean and the perturbations away from the azimuthal mean; $\zeta = (\partial v_t/\partial r) + (v_t/r)$ and $\xi = \zeta + f$ are the relative vorticity and absolute vorticity, respectively; and f is the Coriolis parameter. The first two terms on the right-hand side (RHS) of Eq. (1) are the tangential wind tendencies resulting from the radial transport of the absolute vorticity by the mean radial flow and the vertical advection of tangential wind by the mean vertical velocity. These two terms represent the interaction between the axisymmetric primary circulation and secondary overturning circulation. The third term F_λ is the tendencies from the eddy correlations among the model-resolved asymmetric eddy components of radial, tangential, and vertical winds. The last term F_{sgs_λ} represents the tendency resulting from the parameterized subgrid scale (SGS) turbulence and viscosity in the tangential direction, which is generally negative in the lower BL reflecting the friction induced by turbulence. Likewise, the azimuth-mean radial flow budget equation may be expressed as

$$\frac{\partial \overline{u_r}}{\partial t} = -\overline{u_r}\frac{\partial \overline{u_r}}{\partial r} - \overline{w}\frac{\partial \overline{u_r}}{\partial z} + C - \frac{1}{\overline{\rho}}\frac{\partial \overline{p}}{\partial r} + F_r + F_{\mathrm{sgs}_r}, \tag{2}$$

where ρ and g are the air density and gravity, $C = (\overline{v_t}^2/r) + f\overline{v_t}$, and $F_r = -\overline{u_r'(\partial u_r'/r)} - \overline{v_t'(\partial u_r'/r\partial\lambda)} - \overline{w'(\partial u_r'/\partial z)} + \overline{v_t'^2}/r$. The first two terms on the RHS of Eq. (2) are the tendencies resulting from the radial and vertical advection of mean radial flow. The last four terms represent the centrifugal force $\overline{v_t}^2/r$, Coriolis force $f\overline{v_t}$, radial pressure gradient force $-[(1/\overline{\rho})(\partial\overline{p}/\partial r)]$, and resolved and SGS eddy forcing $F_r + F_{\mathrm{sgs}_r}$, respectively. Neglecting the local change, advection, and eddy forcing, Eq. (2) reduces to the gradient wind balance $C - [(1/\overline{\rho})(\partial\overline{p}/\partial r)] = 0$. While the gradient-wind balance provides a concise framework for understanding the fundamental TC dynamics, it excludes all the unbalanced processes of a TC. One of the objectives of this study is to seek a method to include the radial eddy forcing resulting from turbulent processes in the TC intensification diagnoses.

Assuming that a TC vortex is in a hydrostatic balance $-[(1/\overline{\rho})(\partial\overline{p}/\partial z)] = \overline{\rho}g$ (a validation of hydrostatic balance assumption that holds for a TC vortex using model output is provided in the online supplemental file), and the radial flow is in a quasi-steady condition, further neglecting the mean advection terms, Eq. (2) reduces to

$$C - \frac{1}{\overline{\rho}}\frac{\partial \overline{p}}{\partial r} + F_r + F_{\mathrm{sgs}_r} = 0. \tag{3}$$

Differentiating Eq. (3) with respect to z and differentiating the hydrostatic balance equation with respect to r, respectively, cancelling out the pressure terms, and then applying the equation of state and the definition of potential temperature θ, it yields

$$g\frac{\partial\overline{\chi}}{\partial r}+\frac{\partial[\overline{\chi}(C+F_r+F_{\mathrm{sgs}_r})]}{\partial z}=0,\ \overline{\chi}=\frac{1}{\overline{\theta}}. \tag{4}$$

For $F_r + F_{\mathrm{sgs}_r} = 0$, Eq. (4) reduces to the standard thermal wind relationship. Thus, Eq. (4) may be considered as a generalized thermal wind relationship that holds for the entire troposphere including the BL. The heat budget equation may be written as

$$\frac{\partial\overline{\chi}}{\partial t}+\overline{u}\frac{\partial\overline{\chi}}{\partial r}+\overline{w}\frac{\partial\overline{\chi}}{\partial z}=-\overline{\chi}^2Q,\ Q=\dot{\theta}+F_\theta+F_{\mathrm{sgs}_\theta}, \tag{5}$$

where $\dot{\theta}$ is the diabatic heating and $F_\theta=-\overline{u_r'(\partial\theta'/\partial r)}-\overline{v_t'(\partial\theta'/r\partial\lambda)}-\overline{w'(\partial\theta'/\partial z)}$ and F_{sgs_θ} are the resolved and SGS eddy forcing, respectively. The azimuthal-mean continuity equation may be written as

$$\frac{\partial(\overline{\rho}r\overline{u_r})}{\partial r}+\frac{\partial(\overline{\rho}r\overline{w})}{\partial z}=0. \tag{6}$$

Equation (6) implies that $\overline{u_r}$ and $\overline{w}$ may be expressed in terms of a streamfunction ψ:

$$\overline{u_r}=-\frac{1}{r\overline{\rho}}\frac{\partial\overline{\psi}}{\partial z},\ \overline{w}=\frac{1}{r\overline{\rho}}\frac{\partial\overline{\psi}}{\partial r}. \tag{7}$$

Differentiating Eq. (4) with respect to time, eliminating the time derivatives of $\overline{v_t}$ and $\overline{\chi}$ using Eq. (1) and Eq. (5), and replacing $\overline{u}$ and $\overline{w}$ with the streamfunction ψ Eq. (7), it ends up with an elliptical partial differential equation in the form of

$$B_{rr}\frac{\partial^2\overline{\psi}}{\partial r^2}+B_{rz}\frac{\partial^2\overline{\psi}}{\partial r\partial z}+B_{zz}\frac{\partial^2\overline{\psi}}{\partial z^2}+B_r\frac{\partial\overline{\psi}}{\partial r}+B_z\frac{\partial\overline{\psi}}{\partial z}=A(R,z), \tag{8}$$

where

$$B_{rr}=-g\frac{1}{r\overline{\rho}}\frac{\partial\overline{\chi}}{\partial z},$$

$$B_{rz}=-\frac{1}{r\overline{\rho}}\left\{2\frac{\partial(C\overline{\chi})}{\partial z}+\frac{\partial[(F_r+F_{\mathrm{sgs}_r})\overline{\chi}]}{\partial z}+(F_r+F_{\mathrm{sgs}_r})\frac{\partial\overline{\chi}}{\partial z}\right\},$$

$$B_{zz}=\frac{1}{r\overline{\rho}}\left[\overline{\chi}\eta(f+\zeta)+C\frac{\partial\overline{\chi}}{\partial r}+(F_r+F_{\mathrm{sgs}_r})\frac{\partial\overline{\chi}}{\partial r}\right],$$

$$B_r=\frac{\partial}{\partial r}\left(-\frac{g}{r\overline{\rho}}\frac{\partial\overline{\chi}}{\partial z}\right)+\frac{\partial}{\partial z}\left[-\frac{1}{r\overline{\rho}}\frac{\partial(C\overline{\chi})}{\partial z}\right]-\frac{\partial}{\partial z}\left[\frac{(F_r+F_{\mathrm{sgs}_r})}{r\overline{\rho}}\frac{\partial\overline{\chi}}{\partial z}\right],$$

$$B_z=-\frac{\partial}{\partial r}\left[\frac{1}{r\overline{\rho}}\frac{\partial(C\overline{\chi})}{\partial z}\right]+\frac{\partial}{\partial z}\left\{\frac{1}{r\overline{\rho}}\left[\overline{\chi}\eta(f+\zeta)+C\frac{\partial\overline{\chi}}{\partial r}\right]\right\}$$
$$-\frac{\partial}{\partial r}\left\{\frac{1}{r\overline{\rho}}\frac{\partial[(F_r+F_{\mathrm{sgs}_r})\overline{\chi}]}{\partial z}\right\}+\frac{\partial}{\partial z}\left[\frac{(F_r+F_{\mathrm{sgs}_r})}{r\overline{\rho}}\frac{\partial\overline{\chi}}{\partial r}\right],$$

$$A=g\frac{\partial}{\partial r}(\overline{\chi}^2Q)+\frac{\partial}{\partial z}(C\overline{\chi}^2Q)-\frac{\partial}{\partial z}[\overline{\chi}\eta(F_\lambda+F_{\mathrm{sgs}_\lambda})]$$
$$+\frac{\partial}{\partial z}[(F_r+F_{\mathrm{sgs}_r})\overline{\chi}^2Q],$$

$$\eta=f+\frac{2\overline{v}}{r}.$$

We refer Eq. (8) as the generalized SEE (GSEE) hereafter. For $F_r + F_{\mathrm{sgs}_r} = 0$, Eq. (8) reduces to the classic SEE derived by Smith et al. (2005) and Bui et al. (2009). Despite the fact that Eq. (8) has more complicated coefficients, the equation is still the standard elliptical partial differential equation, similar to the classic SEE, which can be solved numerically provided that the boundary conditions and forcing are known. Once the streamfunction $\overline{\psi}$ is solved, the azimuthal-mean radial flow $\overline{u_r}$ and vertical velocity and $\overline{w}$ can be calculated from Eq. (7). With the solved $\overline{u_r}$ and $\overline{w}$, the tendencies of azimuthal-mean tangential wind resulting from different processes can be readily diagnosed via Eq. (1). Equation (8) is a powerful diagnostic tool since it provides a mathematical way to examine how the secondary circulation changes in response to individual diabatic heating and turbulent eddy forcings.

Shapiro and Willoughby (1982) first used SEE to diagnose the secondary circulation of a TC-like vortex and examined the change of tangential wind in response to differently prescribed diabatic heating at different radii. However, SEE was derived from the strict gradient wind balance; thus, it lacks the ability to diagnose the unbalanced dynamics in TC intensification. A major advantage of Eq. (8) is that it provides a framework for understanding TC intensification beyond the gradient-wind balance. It allows us to diagnose the individual contributions of specific radial eddy forcing resulting from turbulent processes to the total tangential wind tendency of a TC. It should also be pointed out that unlike the tangential eddy forcing $F_\lambda + F_{\mathrm{sgs}_\lambda}$ and diabatic heating Q in SEE, which appear as the independent forcing terms on the RHS of Eq. (8), the radial eddy forcing $F_r + F_{\mathrm{sgs}_r}$ not only serves as a nonlinear forcing term involving with the diabatic heating, i.e., $(\partial/\partial z)[(F_r + F_{\mathrm{sgs}_r})\overline{\chi}^2Q]$ but also appears in the coefficients of Eq. (8), suggesting that there is an important nonlinear interaction among radial eddy forcing, diabatic heating, and the secondary circulation during the intensification of a TC.

3. Numerical experiments

The numerical experiments analyzed in this paper are the idealized TC simulations by the HWRF that are described in Part I of this study (Katz and Zhu 2024, KZ-1 hereafter). The initial vortex has a tropical storm (TS) intensity with an axisymmetric structure. The maximum surface wind speed of 15.0 m s^{-1} is set at the radius of 75 km. The surface tangential wind profile is prescribed using the formula of Wood and White (2011), which is then extended into the vertical using an analytic function proposed by Nolan and Montgomery (2002). The constructed initial vortex is shown in Fig. 4 of KZ-1. In this paper, we present the analysis results from the three sensitivity experiments with differently prescribed turbulent mixing lengths. As summarized in Table 1, the mixing length profiles used in these three experiments have the same asymptomatic length scale of 150 m but different sloping curvatures by varying the shape parameter β.

TABLE 1. Numerical experiments and prescribed mixing length (k: von Kármán constant; z: height).

Experiments	Mixing length $\frac{1}{l}=\frac{1}{l_0}\left(1+\frac{l_0}{kz}\right)^{\beta}$
BASELINE	$l_0 = 150$, $\beta = 1.0$
EXP-SLOPE-1	$l_0 = 150$, $\beta = 0.5$
EXP-SLOPE-2	$l_0 = 150$, $\beta = 1.5$

For details of the experiments and model configuration, please refer to KZ-1.

The vortex in these three experiments underwent different intensification pathways. Figure 2 shows the time evolution of surface maximum wind speeds and sea level storm central pressure during 120 simulation hours from the three experiments. The TC vortex in EXP-SLOPE-1 reaches CAT-5 intensity at the end of 5-day simulation, but the vortex in EXP-SLOPE-2 barely reaches CAT-2 intensity. The physical reasons for the TC-like vortex to undergo different intensification pathways have been thoroughly discussed in KZ-1. Since these experiments are exactly the same except turbulent mixing parameterization via differently prescribed mixing lengths, they provide excellent cases for us to understand how the unbalanced dynamics induced by the turbulent processes in the TC inner core affect TC intensification. The related issues will be explored using the diagnostic method summarized in section 2.

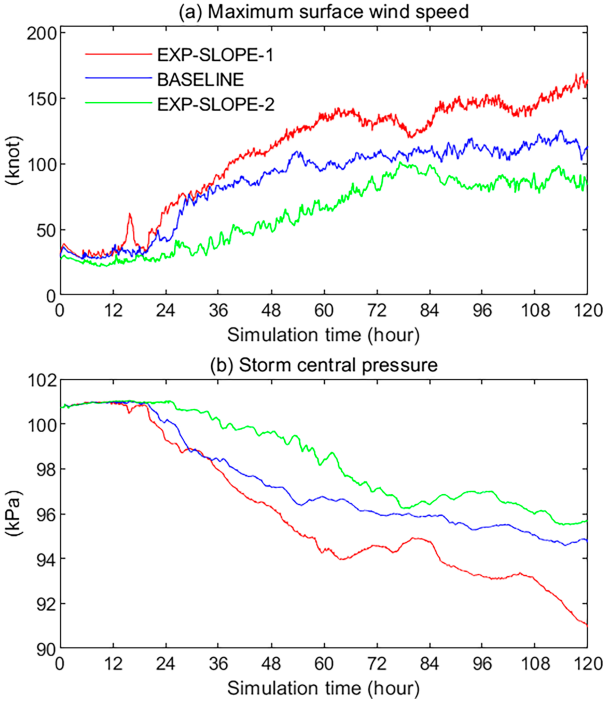

FIG. 2. Time series of surface maximum wind and storm central pressure during 120 simulation hours from EXP-SLOPE-1 (red), BASELINE (blue), and EXP-SLOPE-2 (green).

4. Results

a. Validation of TC secondary overturning circulation diagnosed by SEE and GSEE

Before applying the GSEE diagnostic tool developed in section 2 to analyze the simulated TC intensification, it is important to examine to the extent to which the TC second overturning circulation diagnosed by GSEE can represent the one directly simulated by HWRF. To do so, we carefully compared the simulated azimuthal-mean transverse circulation with those diagnosed by SEE and GSEE during the evolution of the simulated TC vortex. As an example, Fig. 3 shows the simulated azimuthal-mean vertical velocity and radial flow by EXP-SLOPE-1 averaged over the last 24 h compared with the corresponding SEE and GSEE diagnoses. Overall, there is a good agreement between the simulation and diagnoses in terms of the radial-height structure of vertical velocity and radial flow. In particular, the SEE and GSEE diagnoses well capture the location and vertical extension of the eyewall updrafts and the structure of inflow and outflow simulated by HWRF. However, the SEE diagnoses underestimate the magnitude of the eyewall updraft in the midtroposphere around 5–10 km and the outflow, particularly near the tropopause. In the meantime, the SEE diagnoses overestimate the eyewall updraft in the low troposphere and the radial inflow in the BL for both magnitude and radial extension.

The biases shown in the SEE analyses are reduced in the GSEE diagnoses to some extent owing to the inclusion of radial eddy forcing in the analysis. GSEE reduces the overestimated eyewall updraft in the low troposphere by SEE. In particular, GSEE nearly reproduces the magnitude and radial extent of radial inflow simulated by HWRF by cutting down the overestimated inflow by SEE substantially. In addition, GSEE slightly enhances the much-underestimated outflow near the tropopause by SEE. We also calculated the two-dimensional (2D) correlation between the radius–height structure of azimuthal-mean vertical velocity and radial flow simulated by HWRF and the corresponding diagnoses by GSEE and SEE. The results (provided in the supplemental file) show that the 2D correlation coefficients are close to 0.9 for most of the time throughout the simulation period, and GSEE diagnoses are better correlated to the HWRF simulated fields than SEE. However, there are noticeable differences between the simulated fields and SEE/GSEE diagnoses. For example, both SEE and GSEE underestimate the eyewall updraft in the midtroposphere and produce false weak subsidence around the radii of 35–50 km in the BL. These biases could be caused partially by the specified domain boundary conditions when numerically solving SEE/GSEE and partially by the limitation of 2D framework of SEE/GSEE in representing a 3D TC vortex. A detailed discussion on the cause of bias is provided in the supplemental file. Finally, we note that radial flow and vertical velocity affect TC intensification through terms $-\overline{u}_r\overline{\xi}$ (transport of absolute vorticity by radial flow) and $-\overline{w}(\partial\overline{v}_t/\partial z)$ (advection of tangential wind by vertical velocity), respectively, according to Eq. (1). The results of the tangential wind budget analyses (to be shown in the next section) show that $-\overline{u}_r\overline{\xi}$ dominates $-\overline{w}(\partial\overline{v}_t/\partial z)$ (Fig. 4). Thus, we argue that the biases in the azimuthal-mean vertical velocity field should not

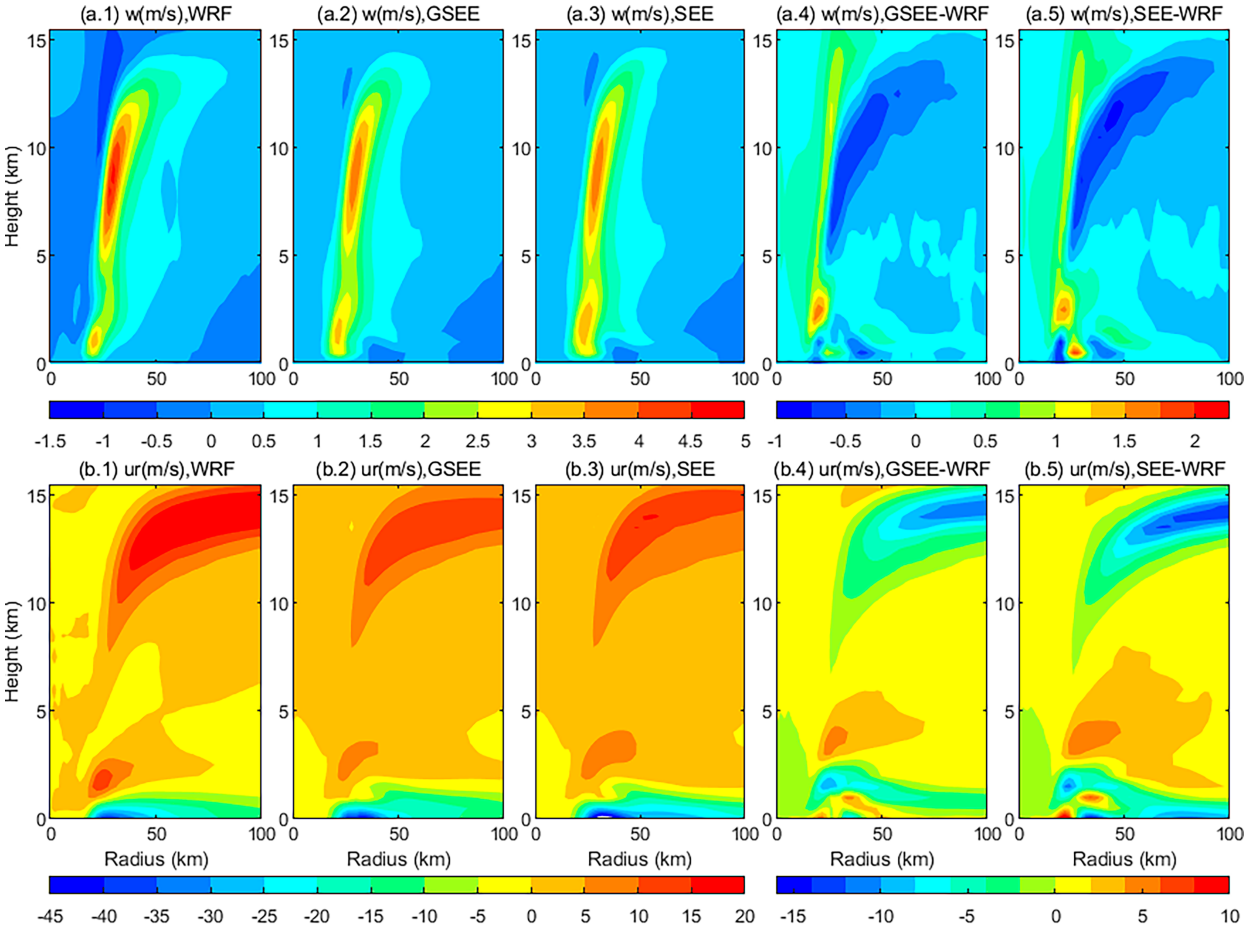

FIG. 3. Comparison of overturning circulation between HWRF simulation and SEE/GSEE diagnoses averaged over the last 24 simulation hours from EXP-SLPOE-1. [a(1)] Azimuthal-mean vertical velocity simulated by HWRF; [a(2)],[a(3)] corresponding vertical velocity diagnosed by GSEE and SEE; [a(4)],[a(5)] bias errors of vertical velocity associated with GSEE and SEE (i.e., GSEE minus HWRF and SEE minus HWRF). [b(1)]–[b(5)] As in [a(1)]–[a(5)], but for radial flow. Note that the white color inside the blue shade in [b(3)] indicates the radial flow exceeds $-45\ \mathrm{m\ s^{-1}}$.

have a substantial impact on the GSEE diagnoses presented in the following sections.

b. TC vortex acceleration in the three experiments

The azimuth-mean tangential wind budget equation (Eq. (1)) provides an excellent way to understand how different dynamic processes contribute to the acceleration of the primary circulation of a TC. Using the model output, KZ-1 presented a detailed tangential wind budget analysis. Figure 4 summarizes the budget analyses of the three experiments. The SGS tangential turbulent eddy forcing F_{sgs_λ} is negative in the inflow layer (Figs. 4a–c), which is the main momentum sink of a TC. The radius–height structure of F_{sgs_λ} is consistent with that of Persing et al. (2013) and Zhu et al. (2019). On the other hand, the radial transport of absolute vorticity ($-\overline{u}_r\overline{\xi}$) generates large positive and negative tendencies in the inflow layer and outflow layer, respectively (Figs. 4d–f). This is easy to understand because $\overline{\xi}$ is positive everywhere, and thus the sign of $-\overline{u}_r\overline{\xi}$ is determined by the radial flow. The peak positive tendency of $-\overline{u}_r\overline{\xi}$ occurs somewhere between the strongest inflow and maximum $\overline{\xi}$ depending on the specific structure of a vortex. Similarly, since $\overline{w}$ is positive in the vicinity of radius of maximum wind (RMW), the sign of $-\overline{w}(\partial\overline{v}_t/\partial z)$ (Figs. 4g–i) is determined by the vertical gradient of tangential wind, which is positive and negative below and above the height of peak tangential wind, respectively. Therefore, $-\overline{w}(\partial\overline{v}_t/\partial z)$ has a sign opposite to $-\overline{u}_r\overline{\xi}$, causing the two terms to cancel each other. However, since the magnitude of $-\overline{w}(\partial\overline{v}_t/\partial z)$ is overwhelmed by $-\overline{u}_r\overline{\xi}$, the net tendency of $-\overline{u}_r\overline{\xi} - \overline{w}(\partial\overline{v}_t/\partial z)$ is to accelerate the primary circulation in the inflow layer near RMW. The tendencies resulting from the eddy correlation of model-resolved asymmetric eddies $-\overline{u_r'\zeta'} - \overline{v_t'(\partial v_t'/r\partial\lambda)} - \overline{w'(\partial v_t'/\partial z)}$ (Figs. 4j–l) are negligible compared to those of the advection terms by the mean flow $[-\overline{u}_r\overline{\xi} - \overline{w}(\partial\overline{v}_t/\partial z)]$. This is consistent with the argument by Nolan et al. (2007) that TC intensification is mainly driven by the TC symmetric response to the azimuthally averaged diabatic heating, rather than to the heating directly associated with individual asymmetries. However, we note that these idealized simulations

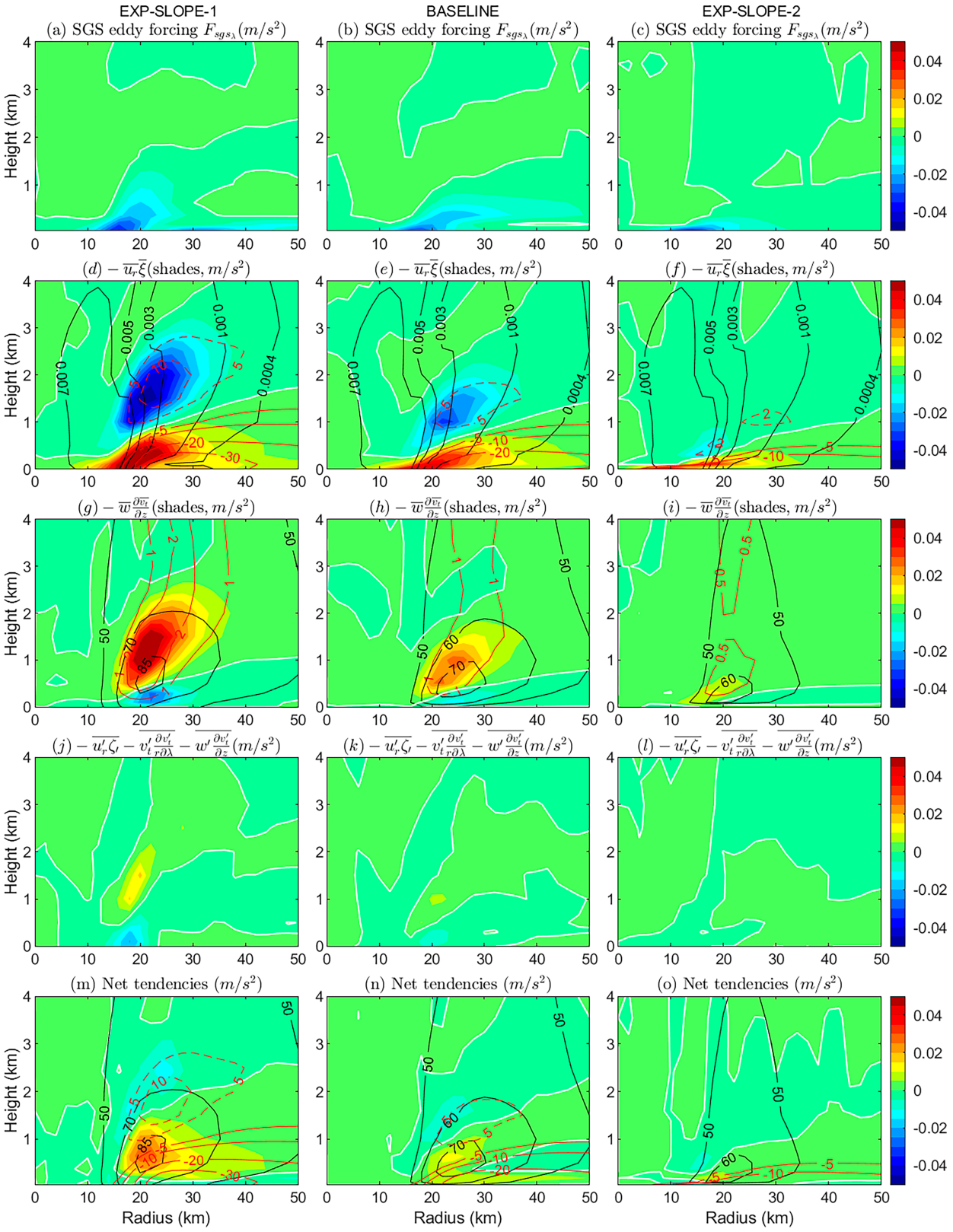

FIG. 4. (first row) Azimuthal-mean SGS tangential eddy forcing F_{sgs_λ} (m s^{-2}) averaged over the last 24 h from EXP-SLOPE-1, BASELINE, and EXP-SLOPE-2, respectively. (second row) As in first row, but for the radial transport of absolute vorticity $-\overline{u_r}\overline{\xi}$ (m s^{-2}).

were performed without ambient wind shear. Previous studies (e.g., Leighton et al. 2018) show that the asymmetric eddies play a larger role in TC intensification in a shear environment. Thus, we expect that $-\overline{u_r'\zeta'} - \overline{v_t'(\partial v_t'/r\partial\lambda)} - \overline{w'(\partial v_t'/\partial z)}$ would be larger if wind shear was prescribed in the idealized simulations.

The tendencies resulting from all terms on the RHS of Eq. (1) are plotted in Figs. 4m–o, which show that the maximum net positive tendency of tangential wind occurs just below the interface between the inflow and outflow near RMW, corresponding well with the peak tangential wind speed. The radius–height structures of the tendency terms are fairly similar among the three experiments. The main difference between them is the magnitude of individual tendency terms, in particular, the radial transport of absolute vorticity $-\overline{u}_r\overline{\xi}$. KZ-1 analyzed how the larger sloping curvature of mixing length in EXP-SLOPE-1 generates the larger $-\overline{u}_r\overline{\xi}$ and kicks off a wind-induced surface heat exchange (WISHE)-like (Emanuel 1986) positive feedback among vortex acceleration via inward transport of absolute vorticity, surface evaporation, radial moisture convergence, and eyewall convection underlying TC intensification.

In short, the results of KZ-1 and Fig. 4 confirm that the inward transport of absolute vorticity is the main driving force for the vortex acceleration. Thus, the goal of this study is to decompose the total $-\overline{u}_r\overline{\xi}$ calculated directly from model output into different components induced by individual processes using GSEE. This decomposition of $-\overline{u}_r\overline{\xi}$ may shed a new light on how these processes contribute to the vortex intensification. While turbulence can affect TC intensification both dynamically and thermodynamically as illustrated in Fig. 1, our focus in this paper will be on the dynamic aspect of how radial and tangential turbulent eddy forcing affects TC intensification.

c. *Role of unbalanced radial turbulent eddy forcing in TC intensification*

The gradient-wind balance provides a concise description of the fundamental TC dynamics. A real TC, however, deviates from the gradient-wind balance due to the turbulent processes, particularly in the BL. To quantitatively measure how far the tangential wind deviates from the balanced gradient wind, we define a quantity known as the normalized net radial forcing (NNRF) as

$$\mathrm{NNRF} = \frac{C - \left| -\frac{1}{\overline{\rho}}\frac{\partial \overline{p}}{\partial r}\right|}{\left| -\frac{1}{\overline{\rho}}\frac{\partial \overline{p}}{\partial r}\right|}. \tag{9}$$

Using the model output, we calculated NNRF. Fig. 5 shows the radius–height distribution of NNRF averaged over the last 24 h from EXP-SLOPE-1, EXP-BASELINE, and EXP-SLOPE-2, respectively. The structure of NNRF from the three experiments shares similar characteristics. The lowest part of the inflow layer is subgradient reflecting the vortex slowing down by the frictional force induced by turbulence. In the outflow core just above the inflow layer, the tangential wind of the vortex is supergradient. The difference among the three experiments is mainly on the magnitude of NNRF. EXP-SLOPE-1 produces much stronger supergradient winds than the other two experiments. The maximum NNRF reaches 0.5. The radial inflow and outflow induced by turbulence and convection are further affected by the radial turbulent eddy forcing F_{sgs_r}. Figure 6 shows the azimuthal-mean F_{sgs_r} from the three experiments. The radius–height structures of F_{sgs_r} from the three experiments are similar. In the inflow and outflow layers, F_{sgs_r} is mainly positive and negative, respectively, reflecting that the SGS turbulence acts as a frictional force to slow down the motion. How radial turbulent eddy forcing affects TC intensification will be discussed shortly.

It is worth noting that the core of positive NNRF in Fig. 5 matches the peak tangential wind well, implying that the supergradient wind may have something to do with the vortex intensification. To further illustrate the relationship between the supergradient wind and vortex tangential wind, Fig. 7 shows the NNRF at the location of the peak tangential winds as a function of the peak tangential wind for the simulation period of 60–120 h from the three experiments. It clearly shows that the peak tangential wind speed is somewhat correlated to its NNRF particularly for the BASELINE and EXP-SLOPE-1 experiments. The poorer correlation between peak tangential wind and NNRF in EXP-SLOPE-2 suggests that the mechanisms governing the vortex intensification in EXP-SLOPE-2 may differ from those in the other experiments. KZ-1 presents a detailed analysis of how the vortex in the three experiments evolves into different intensification pathways from the same initial and environmental conditions. Here, we are looking into this issue from another perspective of how turbulent eddy forcing contributes to the tangential wind tendency using GSEE diagnoses (presented in the following sections).

The somewhat correlated positive NNRF to the peak tangential wind shown in Figs. 5 and 7 raises a question of how the unbalanced dynamics associated with the supergradient and subgradient winds resulting from the radial turbulent eddy forcing affects TC intensification. With GSEE, this question may be adequately addressed by calculating $-\overline{u}_r\overline{\xi}$ induced by the radial eddy forcing. However, as indicated by Eq. (8), the radial eddy forcing $(F_r + F_{\mathrm{sgs}_r})$ does not appear as an independent forcing term but is entangled with the diabatic heating as $(\partial/\partial z)[(F_r + F_{\mathrm{sgs}_r})\overline{\chi}^2 Q]$. Thus, GSEE cannot be

←

(third row) Vertical transport of tangential wind $-\overline{w}(\partial\overline{v}_t/\partial z)$ (m s^{-2}). (fourth row) Tendencies from the resolved eddies. (bottom row) Net tendency of all terms on the RHS of Eq. (1). White contours in all panels indicate zero tendencies. Black contours in the second row are the absolute vorticity (s^{-1}). Black contours in the third and bottom rows are the tangential wind (m s^{-1}). Red solid and dashed contours in the second and bottom rows are the radial inflow and outflow (m s^{-1}), respectively. Red contours in the third row are the vertical velocity (m s^{-1}).

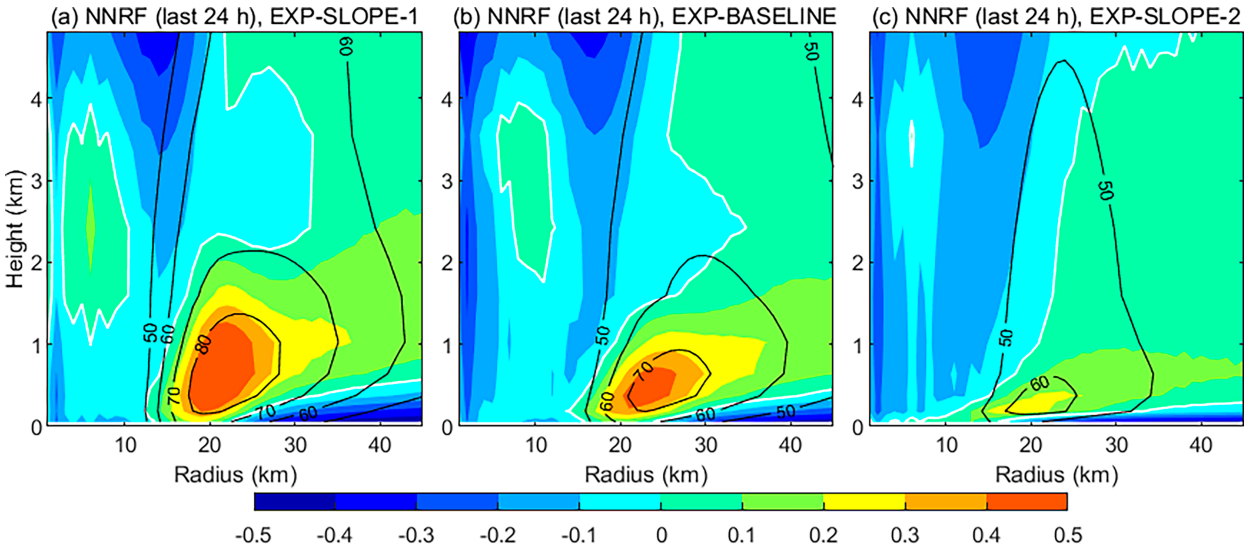

FIG. 5. Radius–height structure of azimuthal-mean NNRF (color shades) and tangential wind (black contours) averaged over the last 24-h simulations from EXP-SLOPE-1, EXP-BASEINE, and EXP-SLOPE-2, respectively. White contour indicates zero NNRF.

forced by $(F_r + F_{\mathrm{sgs}_r})$ alone without diabatic heating. Alternatively, we can solve GSEE and SEE with full forcing (i.e., diabatic heating and tangential/radial eddy forcing for GSEE and diabatic heating and tangential eddy forcing for SEE); then, their difference should tell us the contribution of radial turbulent eddy forcing to the tangential wind tendency via Eq. (1). Moreover, we can further decompose the radial eddy forcing F_{sgs_r} (Fig. 6) into the supergradient and subgradient components based on the positive and negative NNRF (Fig. 5). Using the model output, we performed one set of SEE diagnosis and two sets of GSEE diagnoses (Sup-GW and Sub-GW with supergradient and subgradient components of radial eddy forcing F_{sgs_r}, respectively). Table 2 lists the SEE/GSEE diagnoses along with their forcings. The difference of $-\overline{u}_r\overline{\xi}$ derived from GSEE and SEE diagnoses, then, can be used to identify individually how the radial eddy forcing associated with the supergradient wind and subgradient wind affects the TC intensification.

Figure 8 shows the NNRF and the difference of $-\overline{u}_r\overline{\xi}$ between GSEE (Sup-GW, Sub-GW) and SEE diagnoses averaged over the different time periods throughout the simulation of EXP-SLOPE-1. It clearly shows that the peak tangential wind (indicated by *) falls in the positive regime of $-\overline{u}_r\overline{\xi}$ induced by the radial eddy forcing component associated with the supergradient wind (Figs. 8b.1–b.4) throughout the simulation period, suggesting that the unbalanced dynamics associated with the supergradient wind does contribute positively to TC intensification. The radial eddy forcing

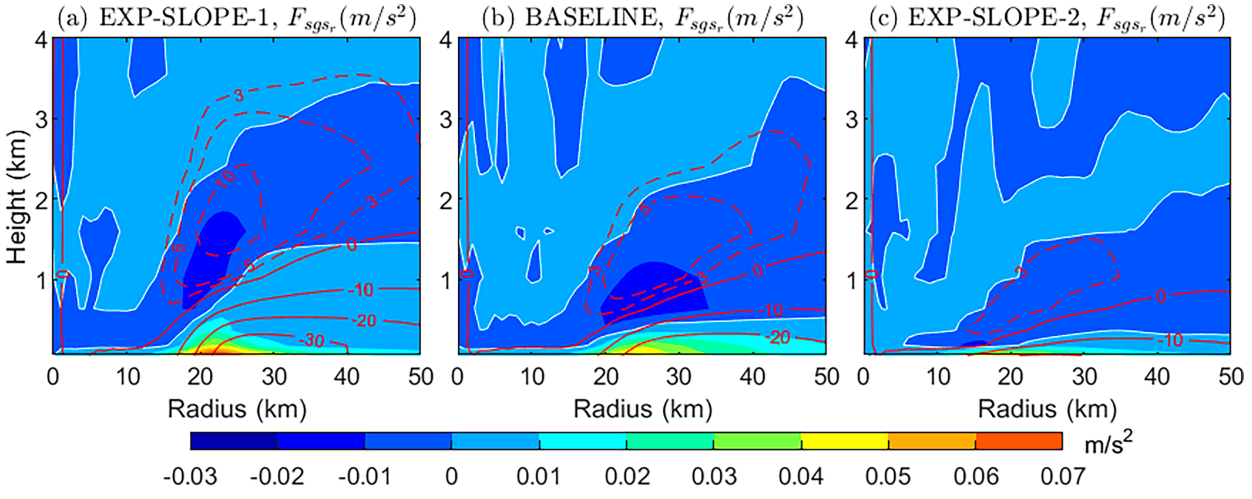

FIG. 6. Azimuthal-mean radial eddy forcing resulting from the parameterized SGS turbulent processes F_{sgs_r} (m s^{-2}) averaged over the last 24 h from EXP-SLOPE-1, BASELINE, and EXP-SLOPE-2, respectively. White contour indicates zero tendencies. Red solid and dashed contours are the radial inflow and outflow, respectively.

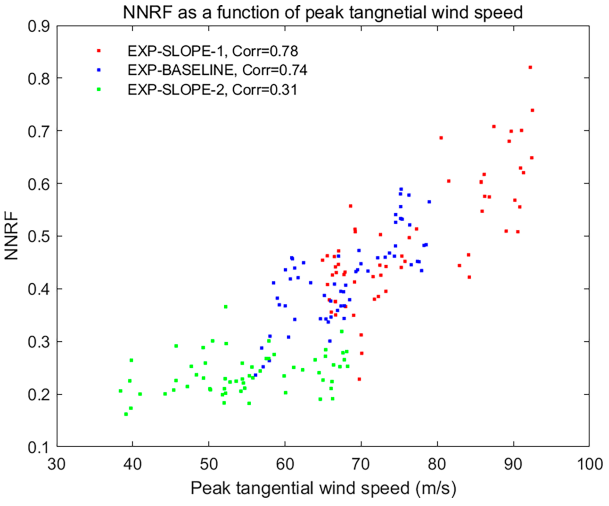

FIG. 7. NNRF at the peak tangential wind as a function of peak tangential wind speed for the simulation period of 60–120 h along with the correlation coefficients between NNRF and peak tangential wind speed from EXP-SLOPE-1, EXP-BASELINE, and EXP-SLOPE-2, respectively.

component associated with the subgradient wind (Figs. 8c.1–c.4), on the other hand, creates positive and negative $-\overline{u}_r\overline{\xi}$ below and above the peak tangential wind, indicating that while accelerating the peak tangential wind, it also tends to lower the height of peak tangential wind. In short, GSEE diagnoses confirm that the unbalanced dynamics associated with supergradient wind and subgradient wind plays a nonnegligible role in TC intensification.

d. *Role of tangential turbulent forcing in TC intensification*

The budget analyses of tangential wind tendency shown in Fig. 4 suggest that dynamically tangential turbulent eddy forcing F_{sgs_λ} can have both negative and positive impacts on TC intensification. Directly, F_{sgs_λ} serves as a frictional force to slow down the primary circulation of a TC as shown in Figs. 4a–8c. This is the well-known effect of F_{sgs_λ}. Indirectly, the weakened tangential winds by F_{sgs_λ} break down the gradient-wind balance and induce the radial inflow, which transports absolute vorticity inward to accelerate the TC vortex. It remains unclear as to which dynamic effect (positive or negative) tends to dominate the other under what conditions. Note that turbulence also transports energy and moisture upward to foster convection. This thermodynamic effect of turbulence on TC intensification will not be discussed in this paper; rather, we focus only on the dynamic effect of turbulence. With GSEE, this issue can be adequately addressed. As shown in Eq. (8), F_{sgs_λ} comes into the equation as an independent forcing term $-(\partial/\partial z)(\overline{\chi}\eta F_{\mathrm{sgs}_\lambda})$; thus, we can force GSEE only with F_{sgs_λ} while setting other forcings to be zero. This will allow us to isolate the component of secondary circulation solely forced by F_{sgs_λ}. Once the radial flow induced by F_{sgs_λ} is diagnosed by Eq. (8), the resultant tangential wind tendency can be calculated by $-\overline{u}_r\overline{\xi}$. Then, the net dynamic effect of F_{sgs_λ} on vortex intensification can be assessed by $-\overline{u}_r\overline{\xi}(F_{\mathrm{sgs}_\lambda}) + F_{\mathrm{sgs}_\lambda}$. Figs. 9 and 10 show the radius–height structures of $-\overline{u}_r\overline{\xi}(F_{\mathrm{sgs}_\lambda}) + F_{\mathrm{sgs}_\lambda}$ averaged over the different time periods throughout the simulations of EXP-SLOPE-1 and EXP-SLOPE-2, respectively. In both experiments, F_{sgs_λ} dominates in the lowest part of the BL and causes the net tendency of $-\overline{u}_r\overline{\xi}(F_{\mathrm{sgs}_\lambda}) + F_{\mathrm{sgs}_\lambda}$ to be negative, consistent with our current knowledge that F_{sgs_λ} is the main momentum sink during the development of a TC. However, there is an interesting difference between the two experiments. In EXP-SLOPE-1, aloft at the height of peak tangential wind (indicated by *), the net tendency of $-\overline{u}_r\overline{\xi}(F_{\mathrm{sgs}_\lambda}) + F_{\mathrm{sgs}_\lambda}$ is in fact positive throughout the simulation (Fig. 9), suggesting that F_{sgs_λ} does contribute positively to the increase of peak tangential wind and favors vortex intensification if considering the indirect dynamic effect of F_{sgs_λ} on tangential wind tendency via $-\overline{u}_r\overline{\xi}(F_{\mathrm{sgs}_\lambda})$.

EXP-SLOPE-2, on the other hand, shows a different story. The radius–height plots (Fig. 10) show that the location of peak tangential wind (indicated by *) falls in the negative regime $-\overline{u}_r\overline{\xi}(F_{\mathrm{sgs}_\lambda}) + F_{\mathrm{sgs}_\lambda}$ from the very beginning when the vortex starts to develop to the end of the simulation, suggesting that the net dynamic effect of F_{sgs_λ} in this case overall is to slow down the tangential wind including the peak tangential wind. The different radius–height structures of $-\overline{u}_r\overline{\xi}(F_{\mathrm{sgs}_\lambda}) + F_{\mathrm{sgs}_\lambda}$ with respect to the peak tangential wind provides an additional reason for why the vortex in EXP-SLOPE-2 behaves differently and fails to intensify like that in EXP-SLOPE-1.

The results shown in Figs. 9 and 10 suggest that the role of tangential turbulent eddy forcing in TC intensification is complex and depends on the details of turbulence parameterization. For the TKE scheme developed from Mellor–Yamada (MY) Level-2 turbulence model (Mellor and Yamada 1982) used in this study, the large sloping curvature of mixing length in EXP-SLOPE-1, which produces the large TKE in the eyewall (KZ-1), causes $-\overline{u}_r\overline{\xi}(F_{\mathrm{sgs}_\lambda}) + F_{\mathrm{sgs}_\lambda}$ to be positive near the location of peak tangential wind, suggesting that the net effect of tangential turbulent eddy forcing plays a role in facilitating vortex intensification in this case. In contrast, in EXP-SLOPE-2 in which the small sloping curvature of mixing length produces the small TKE in the eyewall (KZ-1), the negative effect of tangential turbulent eddy forcing appears to dominate, causing $-\overline{u}_r\overline{\xi}(F_{\mathrm{sgs}_\lambda}) + F_{\mathrm{sgs}_\lambda}$ to be negative near the location of peak tangential wind, which is unfavorable to TC intensification. This result may have important implications in

TABLE 2. SEE and GSEE diagnoses with their forcings.

Diagnoses	SEE	GSEE (Sup-GW)	GSEE (Sub-GW)
Forcings	Q, $F_\lambda + F_{\mathrm{sgs}_\lambda}$	Q, $F_\lambda + F_{\mathrm{sgs}_\lambda}$ $F_r + F_{\mathrm{sgs}_r}$(NNRF > 0)	Q, $F_\lambda + F_{\mathrm{sgs}_\lambda}$ $F_r + F_{\mathrm{sgs}_r}$(NNRF < 0)

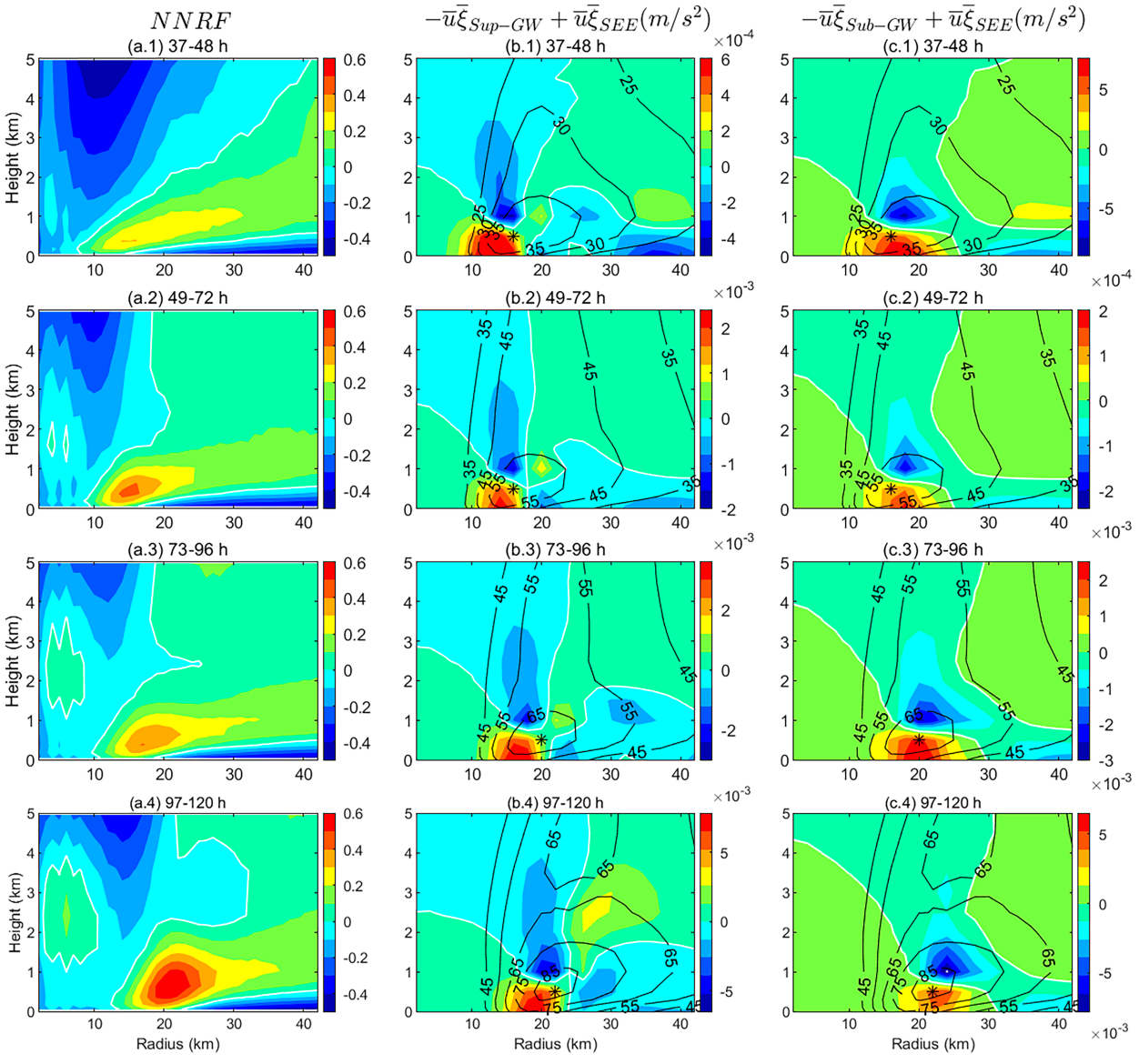

FIG. 8. (a) Azimuthal-mean NNRF; (b),(c) $-\overline{u_r}\overline{\xi}$ derived from GSEE forced by the supergradient and subgradient components of radial eddy forcing subtracted by that from SEE, respectively, averaged over the periods of 37–48, 49–72, 73–96, and 97–120 simulation hours from EXP-SLOPE-1. White contours are the zero tendencies. Black contours are the tangential wind speeds and * indicates the location of peak tangential wind.

real TCs. For intensifying storms, the net effect tangential turbulent eddy forcing could strengthen peak tangential wind if TKEs in the BL and in the eyewall are large, which helps kick off the WISHE-like positive feedback, leading to the rapid intensification of TCs like the case of EXP-SLOPE-1. On the other hand, when TKEs are small like the case of EXP-SLOPE-2, the overall net negative effect of tangential turbulent eddy forcing could be a barrier for TC intensification.

5. Summary and discussion

The importance of the interaction between the primary and secondary circulations of a TC vortex to TC intensification has long been recognized. Under the assumption of gradient-wind balance and hydrostatic balance, by combining the azimuthal-mean tangential wind and heat budget equations, continuity equation, and thermal wind relationship, Shapiro and Willoughby (1982) first derived the so-called SEE, an elliptical partial differential equation that describes the mean secondary overturning circulation of a TC. SEE is a powerful analytical tool that allows for diagnosing how the secondary overturning circulation changes in response to individual diabatic heating and tangential eddy forcing as function of radius and height. To date, SEE has been widely used for understanding TC intensity and structural change including secondary eyewall formation and eyewall replacements

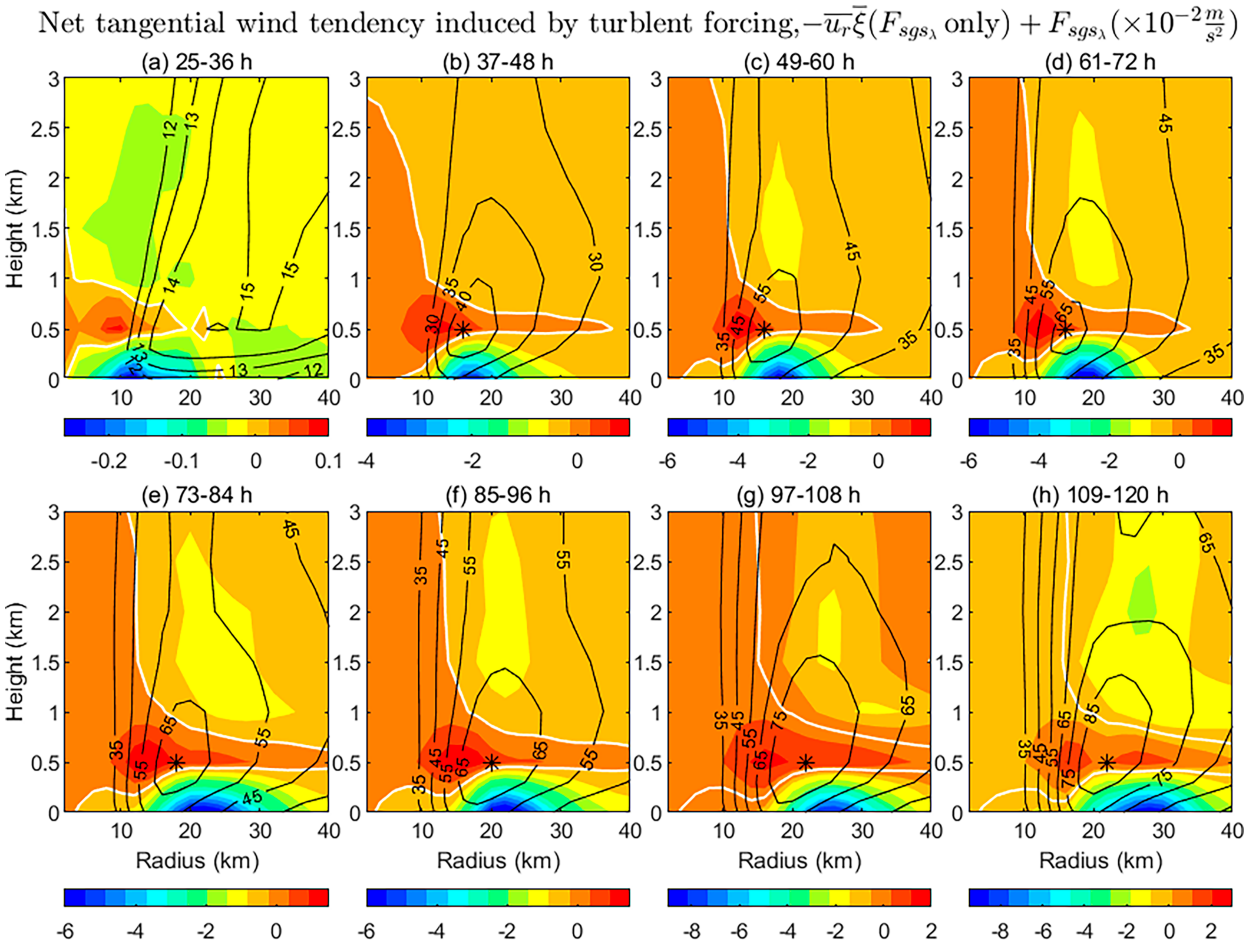

FIG. 9. Net tangential wind tendency induced by the turbulent eddy forcing F_{sgs_λ} only $[-\overline{u_r}\bar{\xi}(F_{sgs_\lambda}) + F_{sgs_\lambda}]$ averaged over the time periods of 25–36, 37–48, 49–60, 61–72, 73–84, 85–96, 97–108, and 109–120 simulation hours from EXP-SLOPE-1. White contours are the zero tendencies. Black contours are the tangential wind speeds, and black star * is the location of peak tangential wind.

(e.g., Smith et al. 2005; Bui et al. 2009; Rozoff et al. 2012; Zhu and Zhu 2014, 2015; Tyner et al. 2018). However, the assumption of strict gradient-wind balance of SEE limits its application in the study of TC evolution, particularly in the BL where the air motion is subgradient due to the slowdown of tangential winds by turbulent friction, and in the outflow region near the top of the BL in the vicinity of RMW where winds are supergradient. While the importance of the unbalanced dynamics caused by turbulence to TC intensification has now been greatly appreciated, the details of how the unbalanced dynamics modulate TC intensification remain poorly understood. To date, no appropriate analytical tool is available to diagnose numerical simulations in an unbalanced framework. This motivates us to develop GSEE by including radial eddy forcing in the analytical framework to remediate the limitation of SEE. Combining GSEE with the tangential wind budget equation, in this study, we diagnosed how tangential and radial eddy forcing affects TC intensification.

The simulations and analyses performed in this study provide a clear physical picture of the multiple roles that the SGS turbulence plays in the TC intensification, which may be schematically illustrated in Fig. 11. First, the SGS tangential turbulent eddy forcing slows down the primary circulation of a TC through the turbulence-induced friction. This is the well-known direct negative effect of turbulence in the tangential direction on a TC vortex. Second, the weakened tangential wind by friction breaks down the gradient wind balance and induces the radial inflow in the BL. As air converges toward the eyewall, it erupts out of the BL, resulting in eyewall updraft. The resultant inward transport of absolute vorticity by the inflow and vertical transport of tangential wind by the eyewall updraft yield opposite signs of tangential wind tendencies and tend to cancel each other. Our budget analyses show that the former dominates the latter, and thus, the induced secondary circulation by turbulence overall has a positive contribution to the acceleration of a TC. This is an indirect positive impact of tangential turbulent eddy forcing on TC intensification. While conceptually the negative and positive dynamic impact of turbulence on the tangential wind tendencies is easy to understand, their net effect on TC intensification is largely unknown. The GSEE diagnostic tool developed in this study allows us to quantitatively address the issue. The diagnostic results show that the relative importance of negative and positive dynamic

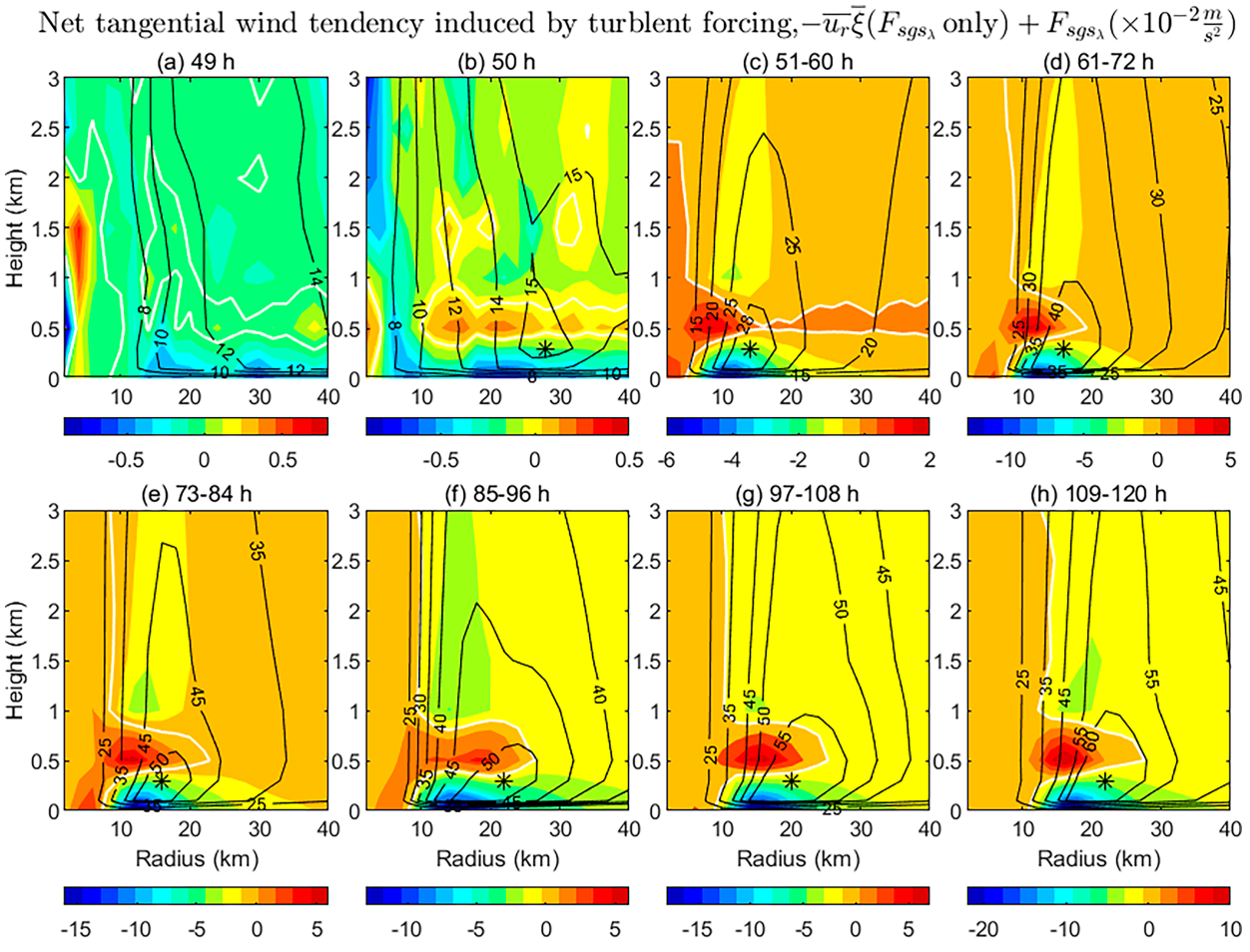

FIG. 10. As in Fig. 9, but for 49, 50, 51–60, 61–72, 73–84, 85–96, 97–108, and 109–120 simulation hours from EXP-SLOPE-2.

effects of tangential turbulent eddy forcing F_{sgs_λ} varies depending on the details of turbulence parameterization. For the MY-Level-2 TKE scheme used in this study, the large sloping curvature of mixing length in EXP-SLOPE-1 yields large TKE in the eyewall (KZ-1), which causes the net effect of tangential turbulent eddy forcing to be positive at the location of peak tangential wind, and thus, it facilitates vortex intensification. In contrast, for the smaller parameterized TKE in EXP-SLOPE-2, the negative effect of tangential turbulent eddy forcing dominates, causing the net effect of tangential turbulent eddy forcing to be negative at the location of peak tangential wind, which is unfavorable to TC intensification.

Third, in addition to the tangential turbulent eddy forcing, the induced radial flow is also subjected to the radial turbulent eddy forcing F_{sgs_r}. How radial turbulent eddy forcing affects TC intensification is an important issue of TC unbalanced dynamics but is not well understood. In this study, we decomposed the radial turbulent eddy forcing F_{sgs_r} into the supergradient and subgradient components based on NNRF. The GSEE diagnoses show that the supergradient component of radial turbulent eddy forcing does contribute positively to the acceleration of tangential winds. The subgradient component, while also accelerating the peak tangential wind, tends to lower the height of peak tangential wind.

Fourth, in addition to the dynamic effect of turbulence, turbulence also transports the energy obtained from ocean surface upward to fuel a TC. The resultant eyewall convection enhances the secondary overturning circulation, which in turn can affect TC intensification in two ways via radial transport of absolute vorticity and vertical transport of tangential winds as discussed earlier. Although these two processes tend to generate opposite signs of tendencies and cancel each other, the tangential wind budget analyses show that the former dominates, and thus, the net effect is to accelerate the TC vortex. The complication is that the secondary circulation component induced by diabatic heating is entangled with radial eddy forcing via term $(\partial/\partial z)[(F_r + F_{sgs_r})\overline{\chi}^2 Q]$ in Eq. (8). Since this study focuses on the dynamic impact of turbulence on TC intensification, we will leave issues of thermodynamic impact of turbulence on TC intensification for our future study.

As summarized previously, TC intensification is delicately determined by a large cancellation among different dynamic and thermodynamic processes. The residue of the cancellation is to cause the maximum acceleration of a vortex and thus the peak tangential wind to occur at the RMW just below the interface between the inflow and outflow (Fig. 11) consistent with dropsonde observations (Zhang et al. 2011). It is also

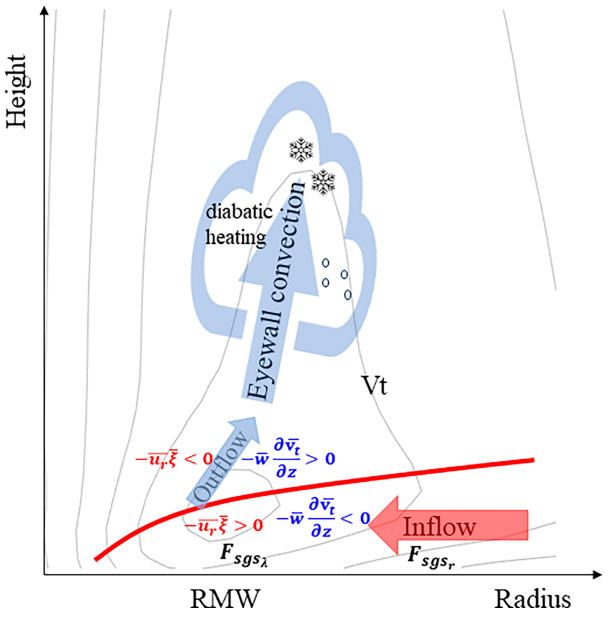

FIG. 11. Schematic illustration of multiple roles that SGS turbulence plays in TC intensification.

clear that all these processes are intimately involved with the turbulence, and thus, changes in turbulence parameterization can alter the cancellation of different physical processes and steer the storm into different pathways to TC intensification. The GSEE developed in this study provides a useful analytical tool for understanding these processes. However, we acknowledge that SEE and GSEE have an intrinsic limitation of describing a 3D TC vortex in a 2D radius–height domain. For the idealized TC simulations in a quiescent condition performed in this study, the impact of this limitation is minimal. For TCs developed in a shear environment, how to appropriately use GSEE to diagnose the development of a TC with a high asymmetry is an issue that needs to be further addressed.

Finally, it should be pointed out that this study focuses only on the issues of vertical turbulent transport in numerical simulations of TCs. In the inner core of a TC, the three-dimensional (3D) turbulent eddies experience large lateral contrasts across the boundaries of eyewall, rainbands, and the moat in-between to yield large lateral turbulent transport comparable to the vertical turbulent transport. Furthermore, lateral entrainment of the unsaturated atmosphere from the moat into the eyewall or rainbands can lead to the entrainment instability, which is an important source of TKE generation in the eyewall and rainband clouds (Zhu et al. 2023). How to appropriately parameterize the comparable interconnected horizontal and vertical turbulent fluxes induced by 3D turbulent eddies in the TC inner core, how to include the lateral entrainment instability in turbulence parameterization, and how 3D turbulent transport affects TC intensification are the important questions that need to be tackled in future research.

Acknowledgments. This work is supported by NOAA/JTTI program under the Grant NA22OAR4590177 and National Science Foundation under the Grant 2211307. We are very grateful to the two anonymous reviewers for their constructive and insightful comments, which led to the improvement of the paper.

Data availability statement. The simulation data generated by this study can be accessed at http://vortex.ihrc.fiu.edu/download/TC_turbulent_processes/.

REFERENCES

Bui, H. H., R. K. Smith, M. T. Montgomery, and J. Peng, 2009: Balanced and unbalanced aspects of tropical cyclone intensification. *Quart. J. Roy. Meteor. Soc.*, **135**, 1715–1731, https://doi.org/10.1002/qj.502.

Emanuel, K. A., 1986: An air-sea interaction theory for tropical cyclones. Part I: Steady-state maintenance. *J. Atmos. Sci.*, **43**, 585–605, https://doi.org/10.1175/1520-0469(1986)043<0585:AASITF>2.0.CO;2.

Katz, J., and P. Zhu, 2024: Parameterization of vertical turbulent transport in the inner core of tropical cyclones and its impact on storm intensification. Part I: Sensitivity to turbulent mixing length. *J. Atmos. Sci.*, **81**, 1749–1767, https://doi.org/10.1175/JAS-D-23-0242.1.

Leighton, H., S. Gopalakrishnan, J. A. Zhang, R. F. Rogers, Z. Zhang, and V. Tallapragada, 2018: Azimuthal distribution of deep convection, environmental factors, and tropical cyclone rapid intensification: A perspective from HWRF ensemble forecasts of Hurricane Edouard (2014). *J. Atmos. Sci.*, **75**, 275–295, https://doi.org/10.1175/JAS-D-17-0171.1.

Mellor, G. L., and T. Yamada, 1982: Development of a turbulence closure model for geophysical fluid problems. *Rev. Geophys.*, **20**, 851–875, https://doi.org/10.1029/RG020i004p00851.

Nolan, D. S., and M. T. Montgomery, 2002: Nonhydrostatic, three-dimensional perturbations to balanced, hurricane-like vortices. Part I: Linearized formulation, stability, and evolution. *J. Atmos. Sci.*, **59**, 2989–3020, https://doi.org/10.1175/1520-0469(2002)059<2989:NTDPTB>2.0.CO;2.

——, Y. Moon, and D. P. Stern, 2007: Tropical cyclone intensification from asymmetric convection: Energetics and efficiency. *J. Atmos. Sci.*, **64**, 3377–3405, https://doi.org/10.1175/JAS3988.1.

Persing, J., M. T. Montgomery, J. C. McWilliams, and R. K. Smith, 2013: Asymmetric and axisymmetric dynamics of tropical cyclones. *Atmos. Chem. Phys.*, **13**, 12 299–12 341, https://doi.org/10.5194/acp-13-12299-2013.

Rozoff, C. M., D. S. Nolan, J. P. Kossin, J. Zhang, and J. Fang, 2012: The roles of an expanding wind field and inertial stability in tropical cyclone secondary eyewall formation. *J. Atmos. Sci.*, **69**, 2621–2643, https://doi.org/10.1175/JAS-D-11-0326.1.

Shapiro, L. J., and H. E. Willoughby, 1982: The response of balanced hurricanes to local sources of heat and momentum. *J. Atmos. Sci.*, **39**, 378–394, https://doi.org/10.1175/1520-0469(1982)039<0378:TROBHT>2.0.CO;2.

Smith, R. K., M. T. Montgomery, and H. Zhu, 2005: Buoyancy in tropical cyclones and other rapidly rotating atmospheric vortices. *Dyn. Atmos. Oceans*, **40**, 189–208, https://doi.org/10.1016/j.dynatmoce.2005.03.003.

——, ——, and N. Van Sang, 2009: Tropical cyclone spin-up revisited. *Quart. J. Roy. Meteor. Soc.*, **135**, 1321–1335, https://doi.org/10.1002/qj.428.

Tyner, B., P. Zhu, J. A. Zhang, S. Gopalakrishnan, F. Marks Jr., and V. Tallapragada, 2018: A top-down pathway to secondary eyewall formation in simulated tropical cyclones. *J. Geophys. Res. Atmos.*, **123**, 174–197, https://doi.org/10.1002/2017JD027410.

Wood, V. T., and L. W. White, 2011: A new parametric model of vortex tangential-wind profiles: Development, testing, and verification. *J. Atmos. Sci.*, **68**, 990–1006, https://doi.org/10.1175/2011JAS3588.1.

Zhang, J. A., R. F. Rogers, D. S. Nolan, and F. D. Marks Jr., 2011: On the characteristic height scales of the hurricane boundary layer. *Mon. Wea. Rev.*, **139**, 2523–2535, https://doi.org/10.1175/MWR-D-10-05017.1.

Zhu, P., and Coauthors, 2019: Role of eyewall and rainband eddy forcing in tropical cyclone intensification. *Atmos. Chem. Phys.*, **19**, 14289–14310, https://doi.org/10.5194/acp-19-14289-2019.

——, A. Hazelton, Z. Zhang, F. D. Marks, and V. Tallapragada, 2021: The role of eyewall turbulent transport in the pathway to intensification of tropical cyclones. *J. Geophys. Res. Atmos.*, **126**, e2021JD034983, https://doi.org/10.1029/2021JD034983.

——, J. A. Zhang, and F. D. Marks, 2023: On the lateral entrainment instability in the inner core region of tropical cyclones. *Geophys. Res. Lett.*, **50**, e2022GL102494, https://doi.org/10.1029/2022GL102494.

Zhu, Z., and P. Zhu, 2014: The role of outer rainband convection in governing the eyewall replacement cycle in numerical simulations of tropical cyclones. *J. Geophys. Res. Atmos.*, **119**, 8049–8072, https://doi.org/10.1002/2014JD021899.

——, and ——, 2015: Sensitivities of eyewall replacement cycle to model physics, vortex structure, and background winds in numerical simulations of tropical cyclones. *J. Geophys. Res. Atmos.*, **120**, 590–622, https://doi.org/10.1002/2014JD022056.